

This is the Accepted Manuscript version of the article accepted for publication:

Zhou, J., Pérez-Grande, D., Fajardo, P., Ahedo, E., (2019), *Plasma Sources Science and Technology*, Volume 28, Number 11 (115004).

IOP Publishing Ltd is not responsible for any errors or omissions in this version of the manuscript or any version derived from it. The Version of Record is available online at <https://doi.org/10.1088/1361-6595/ab4bd3>

ACCEPTED MANUSCRIPT

Numerical treatment of a magnetized electron fluid model within an electromagnetic plasma thruster simulation code

To cite this article before publication: Jiewei Zhou *et al* 2019 *Plasma Sources Sci. Technol.* in press <https://doi.org/10.1088/1361-6595/ab4bd3>

Manuscript version: Accepted Manuscript

Accepted Manuscript is “the version of the article accepted for publication including all changes made as a result of the peer review process, and which may also include the addition to the article by IOP Publishing of a header, an article ID, a cover sheet and/or an ‘Accepted Manuscript’ watermark, but excluding any other editing, typesetting or other changes made by IOP Publishing and/or its licensors”

This Accepted Manuscript is © 2019 IOP Publishing Ltd.

During the embargo period (the 12 month period from the publication of the Version of Record of this article), the Accepted Manuscript is fully protected by copyright and cannot be reused or reposted elsewhere.

As the Version of Record of this article is going to be / has been published on a subscription basis, this Accepted Manuscript is available for reuse under a CC BY-NC-ND 3.0 licence after the 12 month embargo period.

After the embargo period, everyone is permitted to use copy and redistribute this article for non-commercial purposes only, provided that they adhere to all the terms of the licence <https://creativecommons.org/licenses/by-nc-nd/3.0>

Although reasonable endeavours have been taken to obtain all necessary permissions from third parties to include their copyrighted content within this article, their full citation and copyright line may not be present in this Accepted Manuscript version. Before using any content from this article, please refer to the Version of Record on IOPscience once published for full citation and copyright details, as permissions will likely be required. All third party content is fully copyright protected, unless specifically stated otherwise in the figure caption in the Version of Record.

View the [article online](#) for updates and enhancements.

Numerical treatment of a magnetized electron fluid model within an electromagnetic plasma thruster simulation code

J. Zhou, D. Pérez-Grande, P. Fajardo and E. Ahedo

Equipo de Propulsión Espacial y Plasmas (EP2), Universidad Carlos III de Madrid, Leganés, Spain

Email: jzhou@pa.uc3m.es

Abstract

Plasma discharges in electromagnetic thrusters often operate with weakly-collisional, magnetized electrons. Macroscopic models of electrons provide affordable simulation times but require to be solved in magnetically aligned meshes so that large numerical diffusion does not ruin the solution. This work discusses suitable numerical schemes to solve the axisymmetric equations for the electric current continuity and the tensorial Ohm's law in such meshes, when bounded by the thruster cylindrical or annular chamber. A finite volume method is appropriate for the current continuity equation, even when meshes present singular magnetic points. Finite differences and weighted least squares methods are compared for the Ohm's law. The last method is more prone to producing numerical diffusion and should be used only in the boundary cells and requires a special formulation in the boundary faces. In addition, the use of the thermalized potential is suggested for an accurate computation of parallel electron current densities for very high conductivity. The numerical algorithms are tested in a hybrid (particle/fluid) simulation code of a helicon plasma thruster, for different magnetic fields, mesh refinement, and plume lengths. The different contributions to the electric current density are assessed and the formation and relevance of longitudinal electric current loops is discussed.

1 Introduction

The Hall Effect Thruster (HET), the High Efficient Multistage Plasma Thruster (HEMPT), the Applied-Field MagnetoPlasmaDynamic Thruster (AFMPDT), the Helicon Plasma Thruster (HPT) and the gridless Electron Cyclotron Resonance Thruster (ECRT) constitute a family of in-space electric propulsion (EP) technologies, characterized by (i) an axisymmetric geometry, (ii) a weakly-collisional plasma discharge, and (iii) the application of a stationary magnetic field to produce thrust through electromagnetic forces. In all of them the magnetic field guides the electrons and, in combination with the ambipolar electric field, creates Hall-effect azimuthal plasma currents, which produce thrust by interacting with the currents on the external magnetic circuit (made of circular coils, for instance). In addition, the magnetic field confines partially the plasma flow away from the thruster walls and, in the case of magnetic nozzle configurations, is responsible for guiding the plasma flow and partakes in its axial acceleration.

Particle-in-cell (PIC) formulations [1, 2], complemented with Monte Carlo Collisions (MCC) methods [3, 4], are very appropriate for the numerical modeling of the rarefied plasma beam [5, 6, 7, 8]. However, the enormous difference in the particle mass of electrons and ions (typically, constituted of heavy xenon atoms) means that full PIC simulations of the stationary plasma response require very large simulation times, often unsuitable for research and development studies. On the contrary, hybrid simulation codes relying on a PIC-MCC formulation for heavy species and a fluid formulation for electrons present an attractive trade-off between simulation cost and reliability of results [9, 10, 11, 12, 13].

1
2 Fife, Parra, and coworkers [5, 14] developed the hybrid codes HPHALL and HPHALL-2 for HETs,
3 which have been much used afterwards [15, 16]. These codes were designed only for ‘regular’ magnetic
4 topologies, that is with magnetic streamlines connecting inner and outer walls of an annular HET chamber
5 and without singular magnetic points. Nowadays, most new thrusters present more complex magnetic
6 topologies [17, 18, 19], which do not fit within the capabilities of HPHALL-2 or its posterior versions.
7 In particular: modern HET designs tend to implement magnetic shielding of chamber walls [20, 21]; the
8 HEMPT relies on magnetic topologies with several singular points and cusp-type topologies; and the
9 HPT and the ECRT present magnetic nozzles with magnetic lines closing far away from the thruster
10 main chamber [22].

11
12 Mikellides et al. [23, 24, 25] have developed Hall2De, a full-fluid axisymmetric code for HETs, which
13 has been useful in analyzing the plasma response in magnetically shielded HETs such as the Aerojet
14 Rocketdyne XR-5 (previously BPT-4000), or the HERMeS thruster [20, 26]. Hall2De implements a
15 fully 2D treatment of the electron fluid equations on a magnetic field aligned mesh (MFAM or magnetic
16 mesh for short) and is applicable to any axisymmetric magnetic topology. At large values of the Hall
17 parameter, the use of a magnetic mesh is almost mandatory to avoid the strong numerical diffusion
18 between the directions parallel and perpendicular to the magnetic field [27, 28]. [Incidentally, in order to
19 prevent the PIC-related statistical noise, Hall2De opted also for a fluid treatment of heavy species.]

20
21 Within the frame of different research projects, our group is developing HYPHEN, an axisymmetric
22 hybrid multi-thruster simulation tool, with potential application to the family of the five EP technologies
23 cited before. As HPHALL-2, HYPHEN continues relying on a PIC-MCC formulation for ions and neu-
24 trals, which is found much more versatile than the fluid one, taking into account the existence of several
25 heavy species populations (slow and fast ions of charge numbers 0, 1, and 2, at least) and the lack of
26 local thermodynamic equilibrium at low plasma collisionality. For the magnetized electrons, HYPHEN,
27 as Hall2De, attempts to rely on a 2D magnetized fluid formulation implemented on a MFAM.

28
29 As long as the Debye length is the smallest length of the plasma, and plasma quasineutrality holds
30 except in thin Debye sheaths around surfaces, hybrid codes benefit from quasineutrality being easily im-
31 plemented. HYPHEN is thus organized in three main modules: the Ion(I)-module, solving the dynamics
32 of the various ions and neutral species [29, 30, 31], the Electron(E)-module solving the electron response,
33 and the Sheath(S)-module solving the plasma interaction with different types of surfaces (dielectric,
34 metallic,...) [32, 33]. A fourth Wave(W)-module, solving the plasma-wave interaction and energy deposi-
35 tion, is added for thrusters relying on plasma production and heating through electromagnetic emission,
36 such as the HPT and the ECRT [34, 35].

37
38 The goal of this paper is to analyze the numerical algorithms used to solve the electron continuity
39 and momentum equations of the electron fluid on a given MFAM. The strategies for the generation
40 of a suitable 2D magnetic mesh, based on geometric quality indicators, were already discussed in Ref.
41 [28, 33]. The challenges here to obtain accurate numerical algorithms come from several sides: (1) the
42 high irregularity of the cells; (2) the large anisotropy in electron conductivity caused by the magnetic
43 field; (3) the treatment of non-magnetically aligned boundary cells, and (4) the presence of null singular
44 points. Finite volume, finite difference, and least square methods will be proposed for each specific case.
45 Unfortunately, we are not aware of publications on the numerical algorithms on electron equations in
46 Hall2De, which could allow us a comparison with ours.

47
48 The electron continuity and momentum equations are here closed with a polytropic state equation
49 relating pressure and density. To illustrate the electron response with the proposed numerical algorithms
50 a HPT configuration will be used. This will allow to compare the present approach with the simpler one
51 by Ahedo and Navarro [36], where local current ambipolarity is imposed (and ions are treated as a fluid).

52
53 The rest of the paper is organized as follows. Sec. 2 presents the thruster and magnetic geometries
54 that will be simulated and the electron fluid model. Sec. 3 discusses the numerical treatment of these
55 equations. Sec. 4 assesses the previous numerical algorithms treatment with simulations of an HPT
56 plasma discharge. Sec. 5 summarizes the conclusions of this work.

2 Problem formulation

2.1 Geometric and magnetic topologies

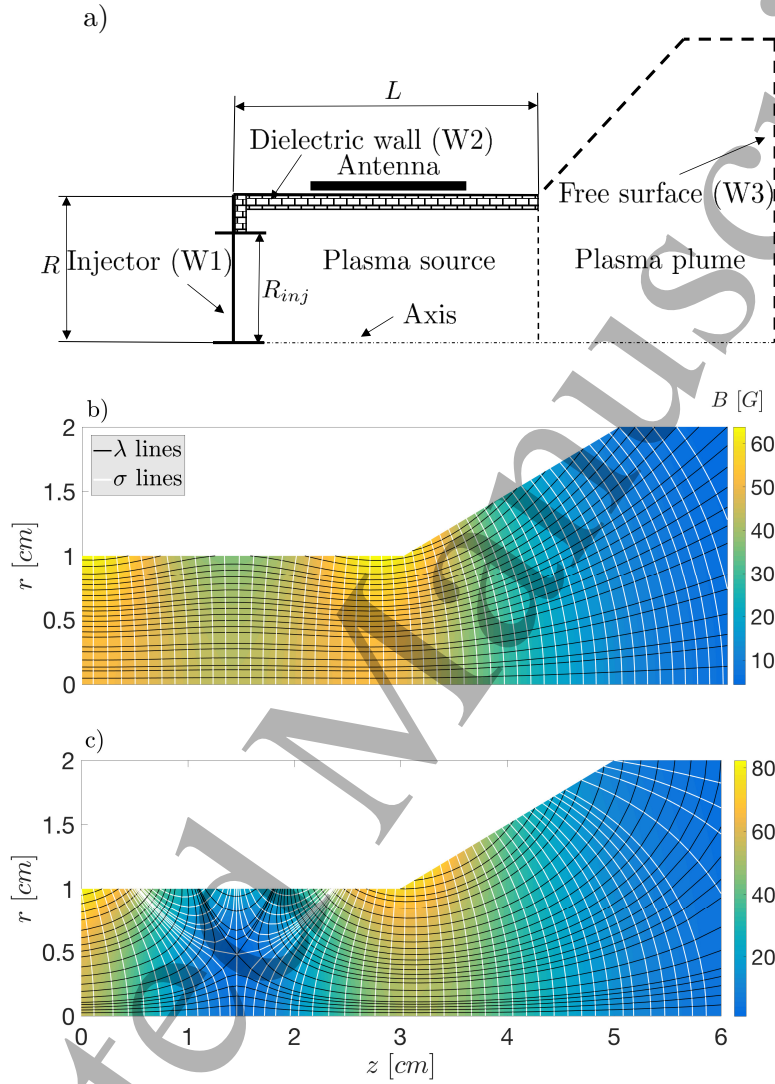


Figure 1: (a) Scheme of the mini-HPT plasma domain to be simulated. The vessel length and radius are 3 cm and 1 cm, respectively. The injector radius is 0.75cm. (b) Conventional magnetic field to be used in cases C1A (and in case C1B with double strength). (c) Magnetic field with a null point used in case C2.

Figure 1(a) presents a sketch of the plasma domain to be simulated, which is similar (but shorter) to the one used in previous HPT studies [34, 36]. The vessel length and radius are $L=3\text{cm}$ and $R=1\text{cm}$. The injector of xenon occupies a circle of radius $R_{inj}=0.75\text{cm}$ at the back of the chamber. The rest of the vessel wall is made of a dielectric material. An external helical antenna around the vessel emits RF energy inside, which is absorbed by the plasma. External coils with independent electric currents generate an applied magnetic field \mathbf{B} . Magnetic topology and strength depend on the values and directions of these currents.

Figure 1(b) and 1(c) depict the streamlines and the equipotential lines (surfaces of revolution, indeed) for two magnetic topologies. Figure 1(b) shows the conventional one for a HPT, with quasi-axial magnetic lines inside the vessel (to accomplish good magnetic confinement at the lateral walls), and divergent

magnetic lines outside (to form the magnetic nozzle that accelerates supersonically the plasma beam and generates magnetic thrust [37, 38]). The topology of Fig. 1(c), bearing a singular magnetic point, has been used in some prototypes [39] and has been selected here mainly to assess the capability of the numerical scheme to deal with a null point.

Two coordinates systems are used: first, the natural cylindrical reference frame $\{\mathbf{1}_z, \mathbf{1}_r, \mathbf{1}_\theta\}$, with coordinates (z, r, θ) ; and, second, the 'magnetic' reference frame constituted by $\{\mathbf{1}_\perp, \mathbf{1}_\parallel, \mathbf{1}_\theta\}$, with $\mathbf{1}_\parallel = \mathbf{B}/B$ and $\mathbf{1}_\perp = \mathbf{1}_\parallel \times \mathbf{1}_\theta$ and coordinates $(\lambda, \sigma, \theta)$. The orthogonal magnetic coordinates $\lambda(z, r)$ and $\sigma(z, r)$ arise from the solenoidal and irrotational equations for the axisymmetric magnetic field, $\nabla \cdot \mathbf{B} = 0$ and $\nabla \times \mathbf{B} = 0$, in an axisymmetric geometry:

$$\frac{\partial \lambda}{\partial z} = rB_r, \quad \frac{\partial \lambda}{\partial r} = -rB_z, \quad (1)$$

$$\frac{\partial \sigma}{\partial z} = B_z, \quad \frac{\partial \sigma}{\partial r} = B_r. \quad (2)$$

The isolines are obtained by numerical integration of these equations and the unit derivatives satisfy

$$\frac{\partial}{\partial \mathbf{1}_\perp} = rB \frac{\partial}{\partial \lambda}, \quad \frac{\partial}{\partial \mathbf{1}_\parallel} \equiv B \frac{\partial}{\partial \sigma}. \quad (3)$$

The selection of a magnetic mesh with a suitable distribution of isolines is a hard task, since the rates of change of λ and σ depend on the local strength of the magnetic field. Hence, the distances between the surfaces defined by two given values of one curvilinear coordinate depend on the field intensity, and can vary widely over the simulation domain. Ref. [28] discussed strategies for meshing definition with a given number of isolines.

2.2 Electron fluid model

According to the sequential and time-marching solving of the models for heavy species and electrons, at each timestep iteration, the I-module delivers 2D maps of densities and fluxes of the different heavy species. This data is implemented into the electron fluid model we describe next, which delivers back the 2D maps of electric potential ϕ , electron current density \mathbf{j}_e , and electron temperature T_e .

Let n_s , Z_s , and \mathbf{u}_s be the density, charge number, and macroscopic velocity of any independent species s (i.e. electrons and different heavy species). Since the plasma is quasineutral, the electron density satisfies

$$n_e \simeq \sum_{s \neq e} Z_s n_s, \quad (4)$$

and is thus known from the I-module. The ion and electron current densities are $\mathbf{j}_i = e \sum_{s \neq e} Z_s n_s \mathbf{u}_s$ and $\mathbf{j}_e = -en_e \mathbf{u}_e$. The first one is computed by the I-module, the second one will be obtained from the continuity equation

$$\nabla \cdot \mathbf{j} = 0, \quad (5)$$

for the electric current density, $\mathbf{j} = \mathbf{j}_i + \mathbf{j}_e$. For these current density vectors, we will distinguish between the azimuthal and longitudinal current densities, that is, for instance, $j_{\theta e} = \mathbf{j}_e \cdot \mathbf{1}_\theta$ and $\tilde{\mathbf{j}}_e = \mathbf{j}_e - j_{\theta e} \mathbf{1}_\theta$.

The electron momentum equation is expressed as

$$\mathbf{0} = -\nabla(n_e T_e) + en_e \nabla \phi + \mathbf{j}_e \times \mathbf{B} + \mathbf{F}_{res}, \quad (6)$$

where the total resistive force, \mathbf{F}_{res} , is modelled as

$$\mathbf{F}_{res} = - \sum_{s \neq e} \nu_{es} m_e n_e (\mathbf{u}_e - \mathbf{u}_s) \equiv \frac{en_e}{\sigma_e} (\mathbf{j}_e + \mathbf{j}_e), \quad (7)$$

with: ν_{es} the collision frequency with species s ; $\sigma_e = e^2 n_e / m_e \nu_e$ the scalar (or parallel) conductivity; $\nu_e = \sum_{s \neq e} \nu_{es}$ the effective electron momentum collision frequency; and

$$\mathbf{j}_c = en_e \sum_{s \neq e} (\nu_{es} / \nu_e) \mathbf{u}_s \quad (8)$$

the heavy species contribution to electron resistivity, expressed, for convenience, in terms of an equivalent current. Just for illustration, if the heavy species in the plasma are reduced to neutrals and singly-charged ions, it is $\mathbf{j}_c \simeq \mathbf{j}_i$ for $\nu_{ei} \gg \nu_{en}$, and $\mathbf{j}_c - \mathbf{j}_i \simeq en_e (\mathbf{u}_n - \mathbf{u}_i)$ for $\nu_{ei} \ll \nu_{en}$.

Finally a polytropic state equation is postulated for T_e :

$$T_e = T_{e0} (n_e / n_{e0})^{\gamma-1}, \quad (9)$$

where γ is the polytropic coefficient and n_{e0} and T_{e0} are two constants. This allows to define the barotropy function

$$h_e = \frac{\gamma(T_e - T_{e0})}{e(\gamma - 1)}, \quad (10)$$

(expressed in the units of ϕ), which satisfies $\nabla h_e = \nabla(n_e T_e) / en_e = \gamma(T_e / e) \nabla \ln n_e$. [For the isothermal case $\gamma = 1$, it is $h_e = (T_{e0} / e) \ln(n_e / n_{e0})$.]

Hence, the momentum equation reads

$$\mathbf{0} = en_e (\nabla \phi - \nabla h_e) + \mathbf{j}_e \times \mathbf{B} + (en_e / \sigma_e) (\mathbf{j}_e + \mathbf{j}_c). \quad (11)$$

which is indeed a tensorial Ohm's law for \mathbf{j}_e . Defining the Hall parameter $\chi = \omega_{ce} / \nu_e$ and setting $\partial / \partial \theta = 0$, the three scalar momentum equations in the magnetic frame can be written as

$$j_{\parallel e} = \sigma_e \left(\frac{\partial h_e}{\partial \mathbf{1}_{\parallel}} - \frac{\partial \phi}{\partial \mathbf{1}_{\parallel}} \right) - j_{\parallel c} \quad (12)$$

$$j_{\perp e} = \frac{\sigma_e}{1 + \chi^2} \left(\frac{\partial h_e}{\partial \mathbf{1}_{\perp}} - \frac{\partial \phi}{\partial \mathbf{1}_{\perp}} \right) - \frac{j_{\perp c} + j_{\theta c} \chi}{1 + \chi^2} \quad (13)$$

$$j_{\theta e} = -j_{\perp e} \chi - j_{\theta c}. \quad (14)$$

Equations (12) and (13) set relation between the electron current density components and ϕ ; the rest of contributions are known from the I-module. Equation (14) does not include ϕ and thus is uncoupled of the other two.

In general it is $L \nu_e (m_e / m_i) \ll \sqrt{T_e / m_i}$ with L the typical chamber dimension. This implies that

$$\frac{\partial \phi}{\partial \mathbf{1}_{\parallel}} \approx \frac{\partial h_e}{\partial \mathbf{1}_{\parallel}} \gg \frac{j_{\parallel e} + j_{\parallel c}}{\sigma_e} \quad (15)$$

and Eq. (12) is ill-conditioned numerically to determine $j_{\parallel e}$. This issue is ameliorated by using, instead of ϕ , the thermalized potential Φ , defined as the correction to the polytropic Boltzmann relation for electrons:

$$\Phi = \phi - h_e(n_e). \quad (16)$$

[Ref. [40] used the Bernoulli function $H_e = -e\Phi$ instead of Φ .] However, in Eq. (13) and for $\chi \gg 1$, we expect

$$\frac{\partial \phi}{\partial \mathbf{1}_{\perp}} \sim \frac{\partial h_e}{\partial \mathbf{1}_{\perp}} \leq O \left(\frac{j_{\perp e} \chi^2}{\sigma_e} \right), \quad (17)$$

so operating with Φ or ϕ is indifferent when solving for $j_{\perp e}$.

Regarding boundary conditions for the electron model, in general, they are set on the current perpendicular to the wall, $j_n = \mathbf{j} \cdot \mathbf{n}$, where \mathbf{n} is the boundary normal unit vector pointing outwards. In particular $j_n = 0$ is imposed at the chamber dielectric walls and at the axis. Since there are no sources of electric current inside the domain, the total current through the free-space boundary is zero. Two limit cases to accomplish this condition are either to take the free-space boundary as 'dielectric' (i.e. $j_n = 0$) or as 'conductor' (i.e. $\phi = \text{const}$). In addition, $\phi = 0$ is set at an arbitrary reference point.

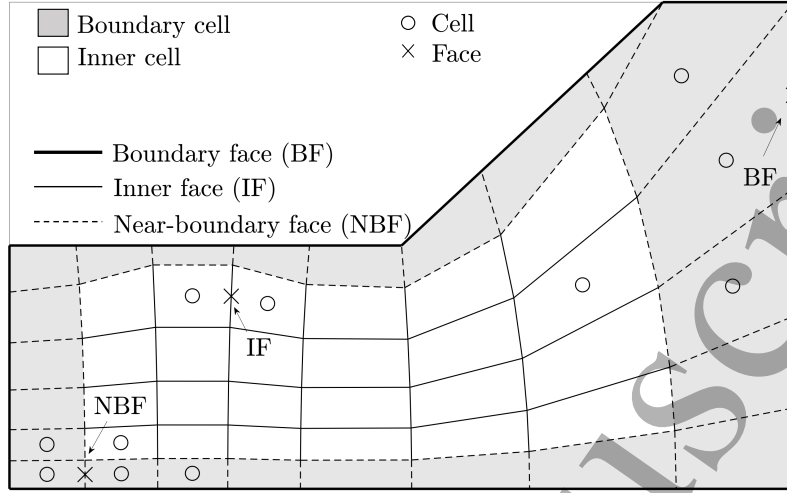


Figure 2: Sketch of cells and faces in a MFAM. The three crosses (\times) are examples of the three types of faces. For each one, the circles surrounding them constitute the stencil considered for gradient reconstruction. The FDM is considered for an inner face. The WLSM is used for the non-inner faces with stencils constituted by two levels of adjacency.

3 Numerical treatment

3.1 Problem discretization

The electron fluid equations will be solved in the magnetic meshes of Fig. 1. A Finite Volume Method (FVM) is chosen to solve the current continuity equation while a Gradient Reconstruction Method (GRM) is used to discretize the Ohm's law for electrons. The cells of the magnetic mesh are divided in two types, sketched in Fig. 2: *inner cells*, enclosed by two pairs of faces that are magnetic lines, and *boundary cells*, with at least one face corresponding to a domain boundary which is not a magnetic line; boundary cells can have a number of faces different from 4. The *cell center* is the magnetic center for the inner cells and the geometric center for the rest of cells. The faces of the magnetic mesh are classified in three types: *inner faces*, separating two inner cells; *boundary faces*, corresponding to the plasma domain boundary; and *near-boundary faces*, which correspond to boundary cells and are not boundary faces. The *face center* is determined by the magnetic center or the geometric center when the former one is not available.

Applying the FVM to the electric current continuity equation on any cell yields

$$0 = \int_{\Omega} d\Omega \nabla \cdot \mathbf{j} \approx \sum_m S_m j_{nm}, \quad j_{nm} \equiv \mathbf{j}_m \cdot \mathbf{n}_m, \quad (18)$$

where Ω is the cell volume, index m applies to all the cell faces, \mathbf{n}_m is the face unit normal pointing outwards, S_m is the area of the cone frustum face (in the 3D axisymmetric space), and \mathbf{j}_m is computed at the center of the face. Except for boundary faces, j_{nm} is either $\pm j_{\parallel}$ or $\pm j_{\perp}$ at the face, while for boundary faces j_{nm} is assumed known (the extension of the numerical method to other boundary conditions is not treated in this work).

GRMs, which are discussed in detail in the next subsection, discretize the derivatives at a face center m of a given function, say the thermalized potential Φ , along a generic direction \mathbf{l} , as a linear combination of the function at several centers of surrounding cells. That is

$$\left. \frac{\partial \Phi}{\partial \mathbf{l}} \right|_m = \sum_l g_{ml} \Phi_l, \quad (19)$$

where l is the index of the cell centers involved, Φ_l are the values at those points, and g_{ml} are the geometric factors of cell l with respect to face m . Using Eqs. (12) and (13) and GRMs, the parallel electric current density at the center of a $\sigma=\text{const}$ face m satisfies

$$j_{\parallel m} = -\sigma_{em} \sum_l g_{ml} \Phi_l + j'_{\parallel m}, \quad j'_{\parallel m} = j_{\parallel im} - j_{\parallel cm}, \quad (20)$$

and the perpendicular electric current density at the center of a $\lambda=\text{const}$ face m is

$$j_{\perp m} = -\frac{\sigma_e}{1+\chi^2} \Big|_m \sum_l g_{ml} \Phi_l + j'_{\perp m}, \quad j'_{\perp m} = \left(j_{\perp i} - \frac{j_{\perp c} + j_{\theta c} \chi}{1+\chi^2} \right) \Big|_m, \quad (21)$$

where current densities related to heavy species and provided by the I-module are included in j'_m .

Acting on all the mesh cells, Eq. (18) leads to the non-square matrix relation

$$A_1 \cdot \{j_{nm*}\} = B_1, \quad (22)$$

with: $\{j_{nm*}\}$ grouping all current densities perpendicular to non-boundary faces m^* , A_1 collecting the areas of these faces; and B_1 grouping all the information at boundary faces ($B_1 = 0$ if all electric current at the boundaries are zero). Then, applying Eqs. (20) and (21) yields

$$\{j_{nm*}\} = A_2 \cdot \{\Phi_l\} + B_2, \quad (23)$$

with $\{\Phi_l\}$ grouping Φ for all cells, B_2 collecting the information on currents j_i and j_c from the I-module, and A_2 containing plasma and geometric information at non-boundary faces. Eliminating $\{j_{nm*}\}$ between the two matrix equations yields

$$A \cdot \{\Phi_l\} = B, \quad (24)$$

with $A = A_1 A_2$ and $B = B_1 - A_1 B_2$. Since A is a square matrix, Eq. (24) is the matrix equation to be solved for the thermalized potential. HYPHEN employs the PARDISO [41, 42] direct solver for parallelized computation of the solution, although other solvers could be implemented (e.g., LIS [43]).

If the problem was to be solved directly for ϕ instead of Φ , the equation to consider would be

$$A \cdot \{\phi_l\} = B', \quad B' \equiv B + A \cdot \{h_e\}, \quad (25)$$

with B' known from the I-module.

3.2 Gradient reconstruction methods

A Finite Difference Method (FDM) is a simple and well-known method that allows a good accuracy in the numerical evaluation of gradients. The order of accuracy achievable by the FDM and the required discrete positions at which the differentiable function must be evaluated are well-defined. The drawback is that the FDM is devised for structured meshes and is unsuitable for unstructured ones. In the present case of an MFAM, the inner cells constitute a structured mesh in the magnetic coordinates but boundary cells (with boundary faces not magnetically aligned) must be treated as in an unstructured mesh and require other GRMs.

The most extended GRMs on unstructured meshes, which are to be used here for non-inner faces, are the Weighted Least Squares Method (WLSM) and the Green-Gauss Method (GGM) [44, 45, 46]. The GGM is based on applying the divergence theorem on a finite volume to establish the relation between the gradient within the said volume with the function values at its edges. Since in our problem derivatives need to be obtained at the cell faces, the application of this method is not direct and a dual mesh of finite volumes or an interpolation scheme must be introduced. This would add unnecessary complexity and unknowns, since the definition of the numerical artifices required for the GGM is not obvious. These reasons ruled out to use the GGM here.

On the other hand, the WLSM is built on Taylor's expansions around a point (a face center here) and it relates the gradients at that point with the values of the variable at a set of surrounding points (cell centers in our case), called the stencil. The number of points of the stencil (number of Taylor's expansions and equations) is generally larger than the number of derivatives to be computed; thus a weighted linear regression is introduced to obtain the solution. The WLSM can be applied straightforwardly to our boundary cells but poses two issues. First, the optimal number and location of stencil points is case-dependent and requires some trials and estimations. Second, since derivatives at different directions are obtained simultaneously, the method is prone to cause numerical diffusion in an anisotropic problem, as it is shown in Appendix A. This last issue explains that, although the WLSM could be applied to all faces within the domain, it has been limited to non-inner faces.

The first-order Taylor's expansion (say for Φ) around face m reads

$$\Phi_l \simeq \Phi_m + \left. \frac{\partial \Phi}{\partial \mathbf{1}_{\parallel}} \right|_m \Delta s_{\parallel ml} + \left. \frac{\partial \Phi}{\partial \mathbf{1}_{\perp}} \right|_m \Delta s_{\perp ml}, \quad (26)$$

where: Φ_l applies to cells l adjacent to face m , $\Delta s_{\perp ml}$ and $\Delta s_{\parallel ml}$ are arc lengths from face m to cell center l . In the FDM, the stencil of points is selected so that they are aligned along one magnetic coordinate, and thus arc lengths along the second coordinate are zero. Here, on an inner face m , a 2-point stencil is used by taking the two inner cells adjacent to said face. The above Taylor's expansion allows to compute Φ and its derivative perpendicular to the face. The associated coefficients g_{ml} in Eq. (19) are $\pm \Delta s_{\parallel ml}^{-1}$ or $\pm \Delta s_{\perp ml}^{-1}$.

On near-boundary faces the WLSM is applied on a stencil that extends until the second level of adjacency; the first level being the cells directly adjacent to the face, and the second level being the cells adjacent to those. This typically means 5-6 cells as it is illustrated in Fig. 2. If the above first-order Taylor expansion with 3 unknowns is considered, the set of equations for the stencil is overdetermined and the WLSM must be applied.

The linear system in Eq. (26) can be formally expressed as

$$\{\Phi_{l_k}\} = C \cdot \mathbf{x}_m, \quad \mathbf{x}_m = (\Phi, \partial \Phi / \partial \mathbf{1}_{\parallel}, \partial \Phi / \partial \mathbf{1}_{\perp})_m \quad (27)$$

with $\{\Phi_{l_k}\}$ extended to the k adjacent cells and C a matrix of geometric coefficients. The WLSM function F to be minimized is

$$F(\mathbf{x}) = [(\{\Phi_{l_k}\} - C\mathbf{x}_m)]^T \cdot W \cdot [(\{\Phi_{l_k}\} - C\mathbf{x}_m)], \quad (28)$$

where superindex T is for the transposed matrix and the elements of the diagonal weighting matrix W have been chosen as $W_{ll} = (\Delta s_{\perp ml}^2 + \Delta s_{\parallel ml}^2)^{-1}$, i.e., the relative weight of each cell is proportional to the inverse of the squared distance to the face. Other weighting methods are possible and have been proposed in the literature; however the inverse square distance allows us to construct gradients that are biased to over-represent local information, which we have found to work best with functions in which large spatial gradients are expected. The solution of the WLSM for \mathbf{x} is

$$\mathbf{x}_m = G \cdot \{\Phi_{l_k}\}, \quad G = (C^T W C)^{-1} C^T W, \quad (29)$$

and one column of G includes the coefficient g_{ml} needed in Eq. (19).

3.3 Magnitudes at the boundary faces

The above GRM yields Φ at all cell centers and the derivatives of ϕ at all non-boundary faces. Interpolating appropriately that data, a complete 2D picture of Φ and \mathbf{j}_e is obtained (for instance at the regular mesh nodes of the I-module), except for the values at the domain boundaries. There, the main difficulty is that data extrapolation in an irregular mesh can yield large errors, as we show next. [Hereafter in this subsection and for sake of illustration we assume $j_{nm} = 0$ at any boundary.]

A first way of determining $\mathbf{x}_m = (\Phi, \partial\Phi/\partial\mathbf{1}_{\parallel}, \partial\Phi/\partial\mathbf{1}_{\perp})_m$ at a boundary face is just applying the previous WLSM using two-adjacency level stencils, resulting of course in Eq. (29). Then, Eqs. (20) and (21) yield the electric current densities at the boundaries as

$$j_{nm} = -\sigma_{e,m} \left(\cos\alpha \frac{\partial\Phi}{\partial\mathbf{1}_{\parallel}} - \frac{\sin\alpha}{1+\chi^2} \frac{\partial\Phi}{\partial\mathbf{1}_{\perp}} \right) \Big|_m + j'_{nm}, \quad (30)$$

with: $j'_{nm} = j'_{\parallel m} \cos\alpha - j'_{\perp m} \sin\alpha$, and $\alpha = \text{angle}(\mathbf{n}_m, \mathbf{1}_{\parallel m})$. The accuracy of this standard WLSM at a boundary face [called WLSM(1)] is very poor due to the combination of large magnetic anisotropy and mesh irregularity. This is illustrated in Fig. 3(a), which plots, for a particular simulation, the relative error $|j_{nm}^{(1)}/j_{i,nm}|$, where $j_{nm}^{(1)}$ is the perpendicular current density provided by the WLSM(1) and $j_{i,nm}$ is the perpendicular ion current density at the boundary.

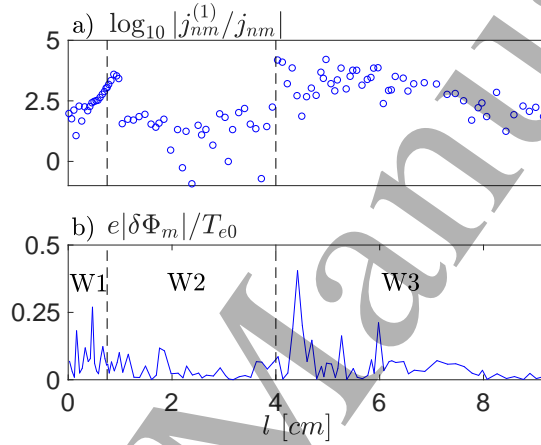


Figure 3: Relative errors in computing magnitudes at the boundary faces with WLSM(1) and WLSM(2). The coordinate l is an arc length parameter that begins at point (0, 0) and increases clockwise along the boundary walls W1, W2, and W3.

A second way of determining \mathbf{x}_m is a modified WLSM [called WLSM(2)], which assures the fulfillment of $j_{nm} = 0$ in Eq. (30). The linear system from Eq. (27) is now expressed as

$$\{\Phi_{l_k} - \Phi_m\} = C_1 \cdot \mathbf{x}'_m, \quad \mathbf{x}'_m = (\partial\Phi/\partial\mathbf{1}_{\parallel}, \partial\Phi/\partial\mathbf{1}_{\perp})_m. \quad (31)$$

The solution of this WLSM(2) is

$$\mathbf{x}'_m = G_1 \cdot \{\Phi_{l_k} - \Phi_m\}, \quad G_1 = (C_1^T W C_1)^{-1} C_1^T W. \quad (32)$$

Substituting the derivatives of Φ from Eq. (32) into Eq. (30) with $j_{nm} = 0$, yields Φ at the boundary face,

$$\Phi_m = \frac{\mathbf{n}' \cdot G_1 \cdot \{\Phi_{l_k}\} - j'_{nm}/\sigma_{e,m}}{\mathbf{n}' \cdot G_1 \cdot \{1\}}, \quad (33)$$

with $\mathbf{n}' = (\cos\alpha, -(1+\chi_m^2)^{-1} \sin\alpha)$ and $\{1\}$ a vector of ones.

Figure 3(b) plots the relative difference in Φ_m between the two previous schemes, $\delta\Phi_m = \Phi_m^{(1)} - \Phi_m^{(2)}$, with superscripts (1) and (2) corresponding to WLSM(1) and WLSM(2), respectively. Since changes of $e\Phi$ across the plasma domain are going to be $O(T_{e0})$, the error on $\Phi_m^{(1)}$ is significant. Furthermore, the error becomes strongly amplified when deriving Φ and multiplying by σ_e , as Fig. 3(a) for the electric current densities have shown.

4 Simulation results

The numerical schemes of Sec. 3 for integrating the electron fluid equations in the MFAM of the E-Module have been tested through several simulations of the mini HPT sketched at Fig. 1. The solutions shown here correspond to run sequentially the E-module and the I-module until a stationary discharge is reached. Simulations with three magnetic fields \mathbf{B} are run: case C1A, with the magnetic field of Fig. 1(b); case C1B, identical to C1A but with double strength of \mathbf{B} ; and case C2, with the magnetic field of Fig. 1(c). In the 3 cases the injector delivers a xenon mass flow rate of $\dot{m}=0.1\text{mg/s}$ (equivalent to an electric current of $e\dot{m}/m_i=73\text{mA}$) with a mean injection velocity of $u_{inj}=300\text{m/s}$ and a temperature of $T_{inj}=0.01\text{eV}$. Based on experimental data [47, 48], a polytropic coefficient $\gamma = 1.2$ is used. The reference temperature is $T_{e0}=8\text{eV}$ and is assigned (arbitrarily) to point $(z, r)=(1.4\text{cm}, 0.4\text{cm})$. Chamber walls, W1 and W2, are dielectric and the condition $j_n = 0$ is imposed at them. For magnetically guided plasmas, appropriate local boundary conditions at the downstream free-loss boundary W3, where the total electric current is zero, are a matter of present debate (see for instance [49] and references therein). For the purposes of the present paper we will just take $j_n = 0$ at W3. Notice that consequently the plasma plume leaving the domain downstream is current-free.

The assessment of the previous numerical algorithms on the electron fluid model is carried out in several ways. First, the thrusting performances of the three simulated cases will be briefly analyzed with the aim of understanding particle and energy balances and checking the physical consistency of the solution. Second, the 2D (z, r) maps of main plasma magnitudes will be discussed, checking again for physical reliability of results. Third, a study of the contributions of the different terms of the electron momentum equation in both magnetically-parallel and perpendicular directions will allow us to better estimate dominant and marginal contributions and thus identify the best numerical treatment. And fourth, the effects of cell size and plume extension will be assessed briefly.

4.1 Performances

Thruster performances, parametric analysis, and design optimization are not direct goals of this paper. Nonetheless, a succinct analysis of the performances of the 3 HPT simulations is still useful for interpretation of the results. Appendix B defines main thruster performance indicators and Table 1 shows them for the 3 simulation cases. A very low thrust efficiency, η_F , is observed in all of them, coming from the very low energy efficiency, η_{ene} (4-14%). Most of the absorbed power is spent in the walls (about 56-61%) and inelastic collisions (35-38%). Poor magnetic confinement explains directly wall losses but also the large inelastic collisions since neutrals are ionized twice, on average. This multiple ionization is evident when observing that the propellant utilization η_u is just moderate (13-60%) while the ratio of the total ion mass production rate versus the injected mass flow rate, $\dot{m}_{i,total}/\dot{m} \equiv \eta_u/\eta_{prod}$ is 144-231%, and we remind that inelastic losses are proportional to $\dot{m}_{i,total}$.

The relevance of magnetic confinement is clear when comparing case C1A to C1B and C2. Doubling the magnetic field from C1A to C1B, implies a better magnetic confinement as confirmed by performances: there is a moderate reduction of energy losses at the walls and a large increase of η_u . This agrees with theoretical and experimental evidence [50, 36, 51, 52, 53]. Furthermore, in configurations C1A and C1B, the lateral wall is partially shielded magnetically but not the back wall. As a consequence, while the dielectric-to-injector surface ratio is 11.4 the dielectric-to-injector energy losses are about 4.6, 2.0 and 5.8 for cases C1A, C1B, and C2, respectively. Confinement of the lateral wall improves from C2 to C1A and C1B, and this is reflected in the relative amount of energy losses at wall W2. Regarding wall W1, there is an increase on losses in case C1B, which seems to be due to the maximum plasma density being placed more upstream. Finally, plume efficiency, η_{plu} , is high in all cases, which means that the magnetic nozzle performs correctly. In fact, the plume divergence semi-angle defined as $\arccos \sqrt{\eta_{plu}}$ is moderate, about 24-26 deg.

	P_a [W]	F [mN]	η_u	η_{ene}	η_{plu}	η_F	η_{prod}	ϵ_{inel}	ϵ_{wall}
C1A	8.36	0.166	0.25	0.07	0.83	0.016	0.14	0.37	$0.56 = 0.10 + 0.46$
C1B	10.57	0.365	0.60	0.14	0.83	0.063	0.26	0.38	$0.48 = 0.16 + 0.32$
C2	7.56	0.108	0.13	0.04	0.80	0.008	0.09	0.35	$0.61 = 0.09 + 0.52$

Table 1: Performance indicators. The two terms in the sums of the last column are the contributions of walls W1 (first term) and W2 (second one).

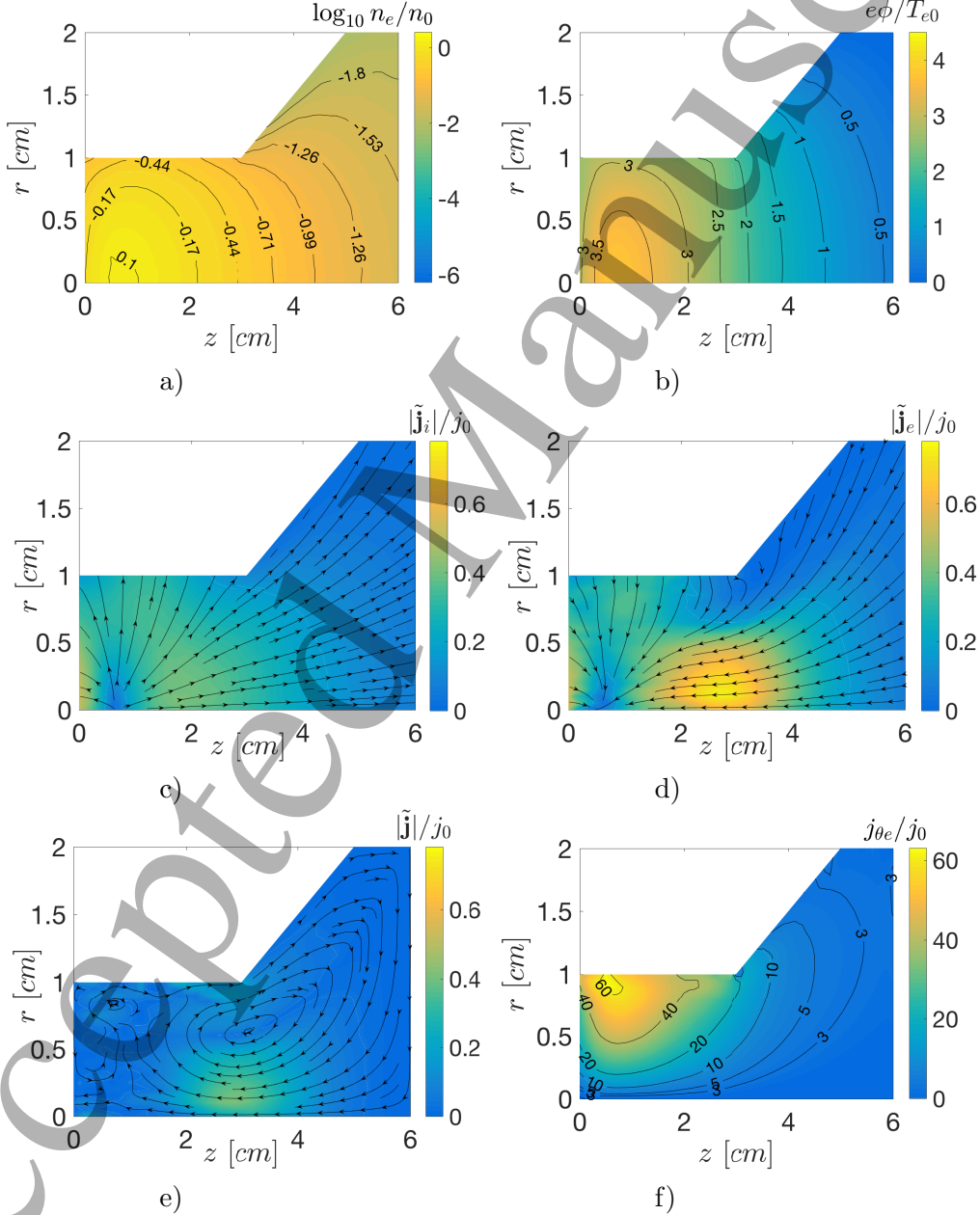


Figure 4: 2D maps of main plasma magnitudes for case C1A. The electron fluid model algorithms are responsible of determining ϕ and \mathbf{j}_e . The I-module provides n_e and \mathbf{j}_i . Plots of plasma properties in this and subsequent figures correspond to a time average of the last 100 timesteps (which correspond to $5\mu\text{s}$ with the time step used) of the stationary solution.

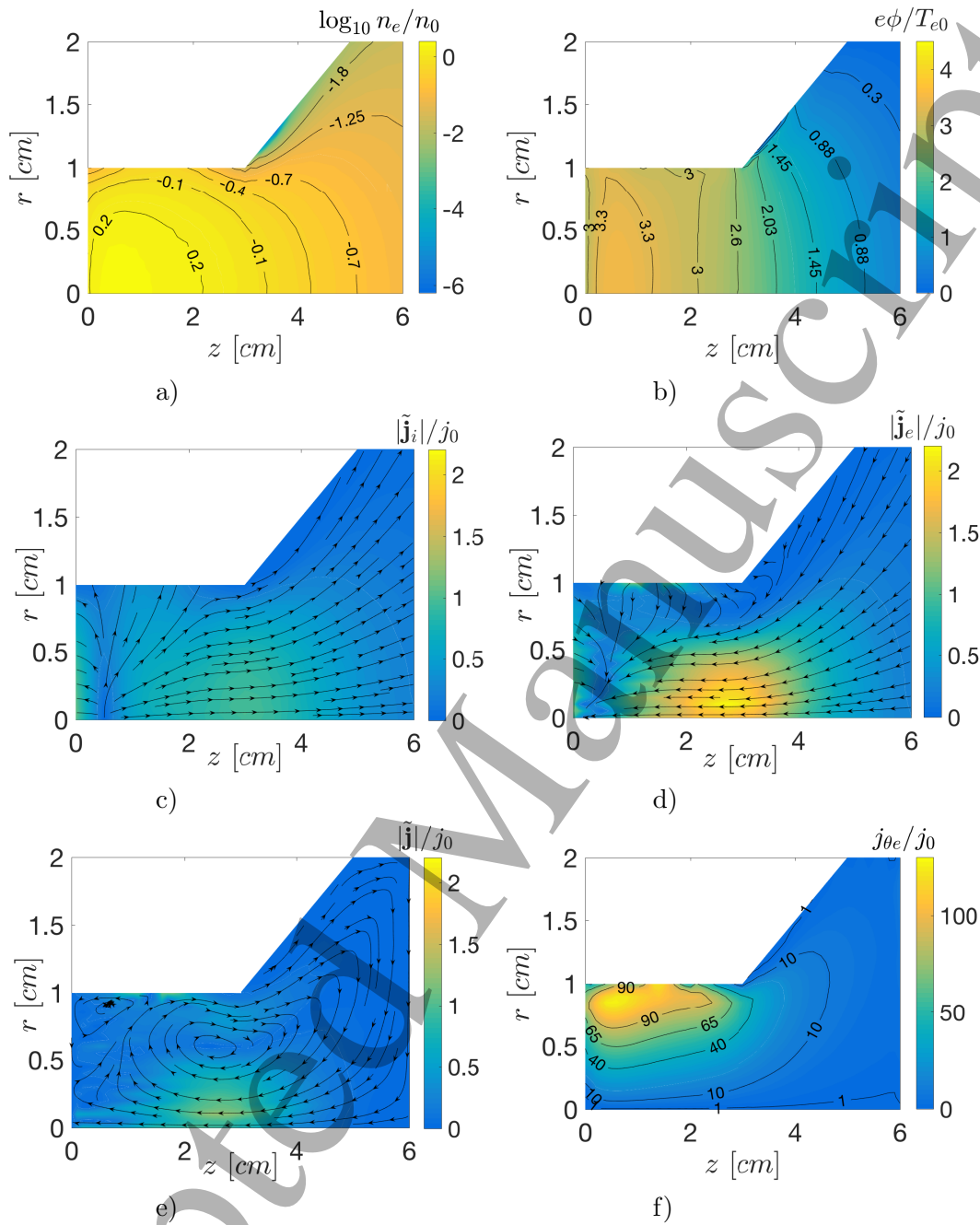


Figure 5: Same than Fig. 4 for case C1B.

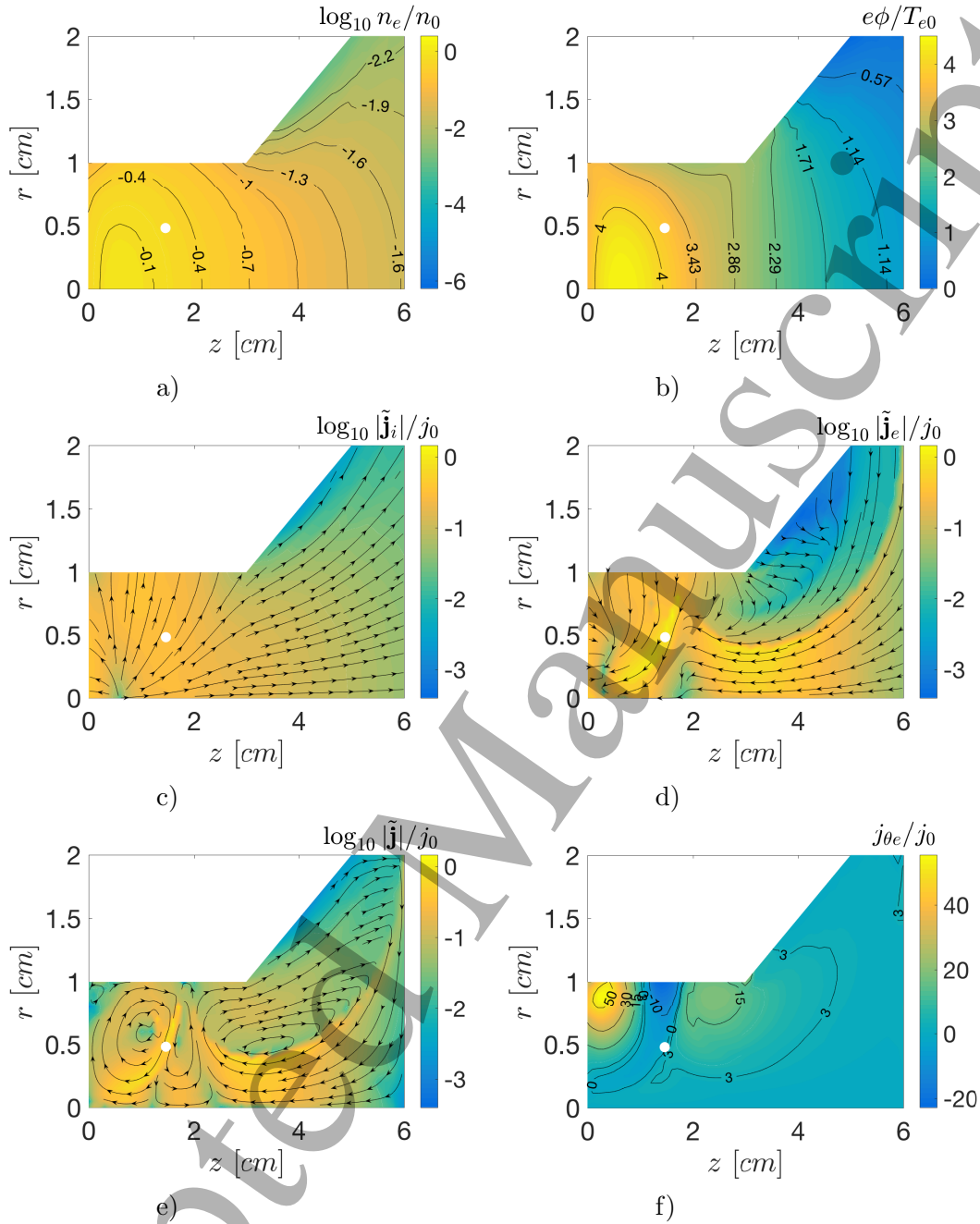


Figure 6: Same than Fig. 4 for case C2. The null magnetic point is indicated with a white dot.

4.2 2D plasma profiles

Figure 4 shows the 2D maps of main plasma magnitudes for case C1A. The map of n_e [subplot 4(a)] comes from the I-module via the quasineutrality condition. Subplot 4(c) for the longitudinal current density \tilde{j}_i is provided by the I-module too. The electron current density vector and the (thermalized) electric potential are the outputs of the present electron fluid model. The reference values used for the dimensionless parameters are

$$j_0 = \frac{\dot{m}}{m_i \pi R^2} = 234 \text{ A/m}^2, \quad c_{s0} = \sqrt{\frac{T_{e0}}{m_i}} = 2.43 \text{ km/s}, \quad n_0 = \frac{j_0}{ec_{s0}} = 6.02 \cdot 10^{17} \text{ m}^{-3}.$$

The ionization rate is maximum around the maximum of n_e (i.e. close to $z=0.5\text{cm}$ and the axis).

This explains also the behavior of the ion current streamlines \tilde{j}_i . The location of the maximum ionization rate near the back of the chamber is going to imply that many ion and electron streamlines end at the chamber walls, explaining the large energy losses and plasma recombination there. Ions move guided by the electric potential ϕ [subplot 4(b)] which satisfies Eq. (16). Since the thermalized potential turns out to be much smaller than the electric potential [see Fig. 7(d) below], ϕ satisfies approximately a ‘polytropic Boltzmann’ relation with the plasma density $\phi \simeq h_e(n_e)$.

The wall-normal electric current density j_n has been taken zero at all domain boundaries. This explains that the maps of $\tilde{j}_e(z, r)$ and $\tilde{j}_i(z, r)$ [Fig. 4(c) and 4(d)] are similar but not identical: a nonzero longitudinal electric current density \tilde{j} [Fig. 4(e)] develops. This feature will be further discussed in a later subsection.

Since ions have a negligible azimuthal motion, the map of $j_{\theta e}$ [Fig. 4(f)] corresponds to the azimuthal electric current density created in the plasma. These circular loops have an intensity proportional to the Hall parameter times $j_{\perp e}$ and a diamagnetic character (i.e. the electric current runs in opposite direction to the coil currents creating \mathbf{B}) [50, 22]. Their interaction with the electric currents in the coils leads to action-reaction axial forces: the loops located in the magnetic nozzle constitute the source of magnetic thrust [22] while those inside the chamber do not contribute practically to thrust.

Figure 5 illustrates the electron fluid behavior for case C1B, where the magnetic strength has been doubled compared to C1A. Although performances improve much, only mild differences are appreciated in the 2D maps. Since the propellant utilization is larger, the plasma density is larger and, as a consequence, all the current densities are larger too. The maximum plasma density is shifted a bit upstream, possibly due to the higher ionization. The topology of current streamlines is very similar to C1A except for mild differences near the chamber walls due to better confinement.

Figure 6 corresponds to case C2. Comparing it with case C1A, the lower propellant utilization leads to a lower plasma density but its general 2D shape is similar; some differences are observed in the profiles of the electric potential inside the chamber. Current densities are naturally lower than in C1A, but the most interesting feature are the differences in the longitudinal currents: observe the three \tilde{j} -loops, the larger twisting of \tilde{j} lines, and the changes of signs of $j_{\theta e}$ (around the separatrices departing from the singular null point). In addition, the gentle behavior of the electric potential and the electron current density around the singular magnetic point (where the electron fluid becomes locally unmagnetized) confirms the capability of the numerical scheme to deal correctly with such points.

4.3 Assessment of the momentum equation terms

The different terms of the electron momentum equations are evaluated in Fig. 7 for case C1A. Panel 7(a) shows that the contribution of heavy species to $j_{\parallel e}$ through $j_{\parallel c}$, Eq. (12), is significant in certain regions of the plasma domain. On the contrary, the contribution of heavy species to the perpendicular electron current density, Eq. (13), is totally negligible: $j_{\perp c}/[(1 + \chi^2)j_{\perp e}] < 10^{-4}$ in case C1A.

Panel 7(b) compares the electric current density to the ion and electron current densities, showing that $|\tilde{j}| \ll |\tilde{j}_e| + |\tilde{j}_i|$ in most parts of the domain, but not everywhere (specially near some boundaries). Then, panel 7(c) compares the parallel and perpendicular electron current densities, showing that they are of the same order inside the chamber (where boundary conditions have a stronger effect), contrary to the naive idea that the anisotropic conductivity leads necessarily to $j_{\perp e} \ll j_{\parallel e}$. In the magnetic nozzle region, the higher Hall parameter and the smaller effect of domain boundaries do lead to the parallel current to dominate. Panel 7(d) plots the map of the thermalized potential Φ . This has variations of about 10% of ϕ variations, which confirms that the electric potential follows approximately a polytropic Boltzmann relation, $\phi(n_e)$. However, this small Φ is crucial to determine the parallel electron current density in a weakly-collisional electron fluid, both in the present magnetized case and in the unmagnetized one [54]. In the magnetized case, Φ is practically constant along the magnetic lines with $\partial\Phi/\partial\mathbf{1}_{\parallel} \ll \partial\Phi/\partial\mathbf{1}_{\perp}$, which makes more challenging the accurate computation of Φ and $j_{\parallel e}$ (this one is the product of the small $\partial\Phi/\partial\mathbf{1}_{\parallel}$ times the very large parallel conductivity σ_e).

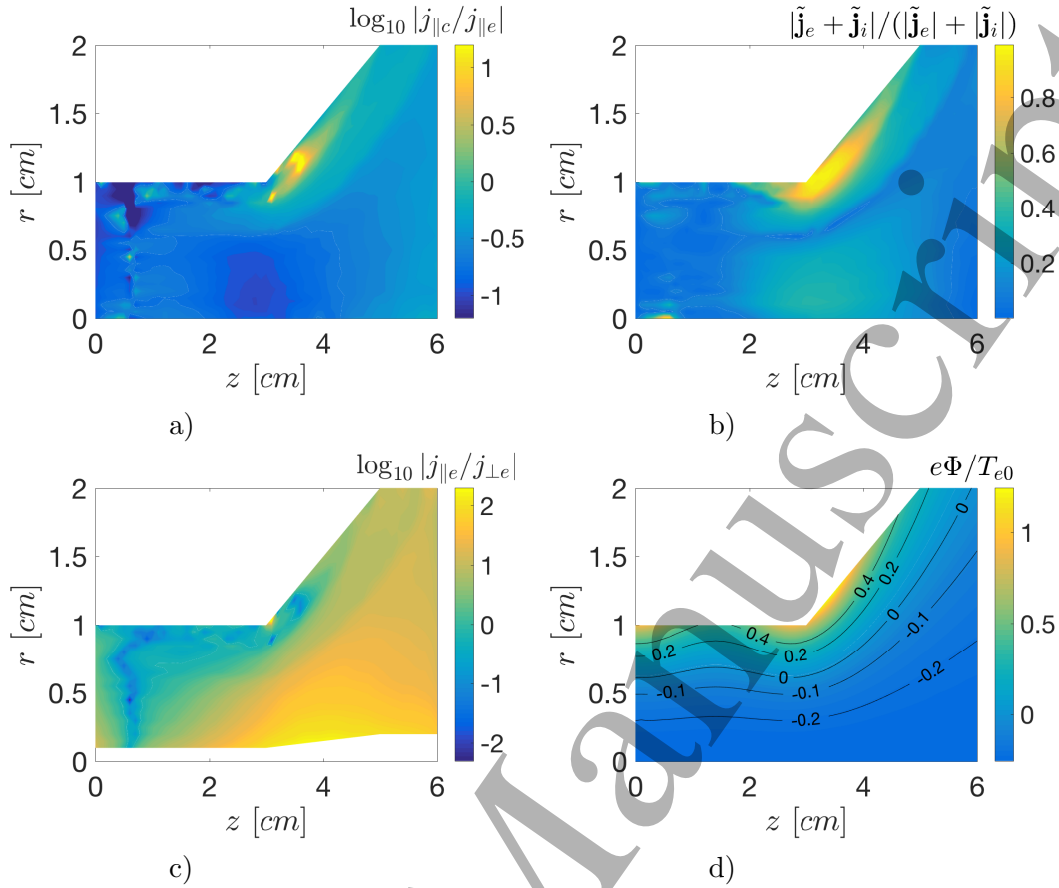


Figure 7: Additional 2D maps of case C1A for the analysis of the terms in the electron momentum equation. Upper and lower bounds have been imposed to the color scale to highlight main features.

A reliable computation of Φ and $j_{\parallel e}$ was the reason to work on the highly irregular MFAM and to use algorithms discretizing $j_{\parallel e}$ and $j_{\perp e}$ independently. Figure 8 compares the electric current densities inside the chamber for C2 when using for inner faces either (a) the FDM or (b) the WLSM; in both simulations, the WLSM is used in non-inner faces. The differences are very noticeable, particularly near the singular point, where the WLSM is unable to reproduce well the two current loops and yields too large values of the electric current density.

Finally, Fig. 9 compares results on the electric current density inside the chamber when either Φ [Eq. (24)] or ϕ [Eq. (25)] are used as main variable in the numerical algorithms. In this comparison, the differences are noticeable, the use of Φ leads to better-defined current streamlines and lower noise in the values of the electric current. It must be mentioned that the temperature T_{e0} was doubled in this simulation to increase the effect of the electron pressure and thus the difference $\phi - \Phi = h_e \propto T_{e0}$.

4.4 On current ambipolarity and plume extension

In previous subsections, we have found that longitudinal electric currents develop in the otherwise current-free plasma beam. These currents form several loops, which are framed by the boundaries of the simulation domain, due to the condition $j_n = 0$ applied there.

This issue of current ambipolarity (i.e. $\tilde{\mathbf{j}} = \mathbf{0}$) in a current-free plasma beam was carefully studied by Ahedo and Merino [22, 55, 56] in the context of a divergent magnetic nozzle (i.e. the plume region in the present case). They showed that fulfillment of current ambipolarity in the divergent nozzle was only achievable if ions (and thus electrons) are fully-magnetized, a too ideal case. For the case of inter-

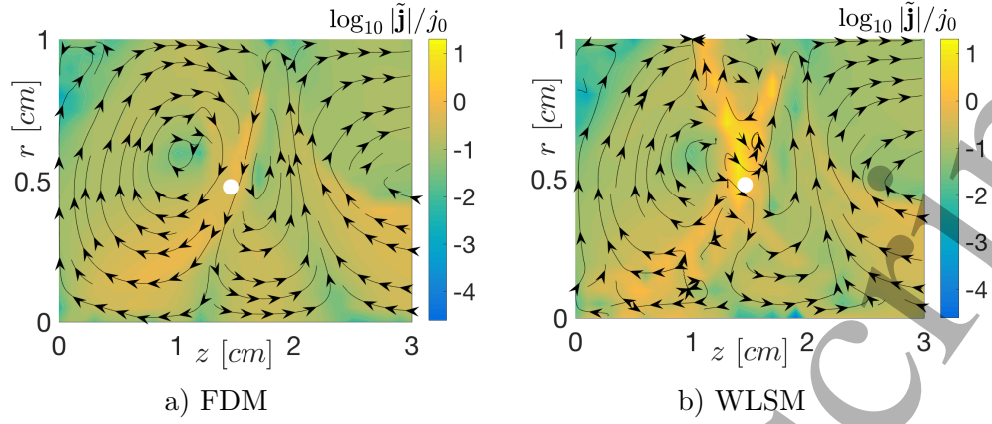


Figure 8: Electric current densities inside the chamber for case C2: (a) the FDM is used in inner faces, (b) the WLSM is used in all faces. The white dot indicates the location of the magnetic null point.

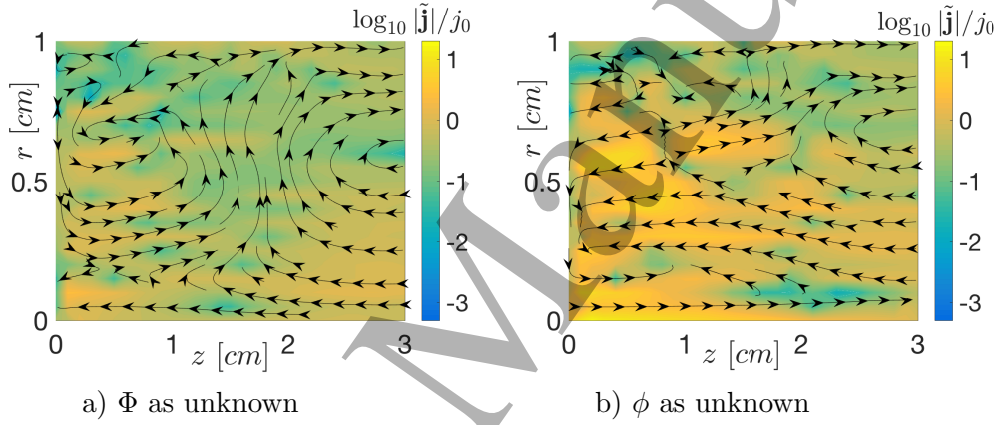


Figure 9: Electric current densities inside the chamber for same magnetic field than case C1A but with $T_{e0} = 16\text{eV}$ (i.e. doubling the T_e map). Numerical algorithms on the electron momentum equation are applied directly on (a) Φ or (b) ϕ .

est of partially-magnetized (or unmagnetized) ions, current ambipolarity cannot be achieved (except at particular surfaces) and its failure is linked to the detachment of ions from magnetic lines [22]. In the present case, which includes thruster chamber and nozzle, we find that longitudinal current loops develop inside the chamber too. This implies that the simplified 2D fluid model (with the magnetic field purely cylindrical) of Ahedo and Navarro [36] for a helicon plasma thruster, which assumed current ambipolarity inside the thruster chamber, was incorrect in that postulate.

However, although the formation of longitudinal currents in the thruster chamber and nozzle is an interesting physical feature, Ahedo and Merino [22, 56] concluded that these currents have almost no relevance on the thruster performances. On the one side, these longitudinal currents induce an azimuthal magnetic field much smaller than the longitudinal field induced by the much higher azimuthal currents [Fig. 4(f) for instance], and even this last induced field is negligible for the plasma densities considered here. On the other side and more relevant for the present discussion, Ahedo and Merino found that, in the *collisionless limit*, $u_{\parallel e}$ (and therefore $j_{\parallel e}$) is a plasma variable uncoupled from the rest. As a consequence, changes of j_n at the downstream boundary, for instance, are mainly managed by $j_{\parallel e}$, affecting minimally the rest of the plasma response.

In order to verify that this behavior continues to apply in the present, more general model, simulations of case C1A with plume axial lengths from 3 cm (in the nominal case of Fig. 4) to 4.5 cm and 6 cm have been run. As the condition $j_{n,W3} = 0$ is moved downstream with the plume length, the most downward

longitudinal current loop changes length and topology. Figure 10 (a) and (b) show the ion and electric current densities for the 4.5cm-plume (i.e. 7.5 cm of total domain extension); plots have been restricted to $z \leq 6$ cm in order to compare them easily with Fig. 4 (c) and (e). Differences are observed in $\tilde{\mathbf{j}}$, but there are practically no changes on $\tilde{\mathbf{j}}_i$, and the same is true for n_e and ϕ (not shown in the figure). Also, thruster performance indicators remain basically the same for the three plume lengths, with differences about 1-2% (which, in fact, is about the level of noise of PIC simulations). Fig. 10(c) shows, at the mean radius for each $z = \text{constant}$ section, the 1D profiles of $|\tilde{\mathbf{j}}_i|$, $j_{\perp e}$, and $j_{\parallel e}$ for the three plume lengths. Observe that differences are only relevant on $j_{\parallel e}$ and even these tend to fade out if the plume is long enough. This completes the confirmation of the validity, in this more general case, of Ahedo and Merino's conclusions relative to the relevance of longitudinal electric currents in a magnetically guided plasma beam.

Finally, the preceding analysis allows us also to assess the effects of simulating a truncated plasma plume on the plasma/thruster response. As long as this length is not too short, the effects turn out to be rather marginal. Furthermore, Ahedo and Merino's theory and the present analysis suggest that the conditions set at the downstream boundary W3 (either $j_n = 0$ or a different one on the electric current or potential) seem to be scarcely relevant on the plasma response, except for the parallel electron current and the related longitudinal electric currents.

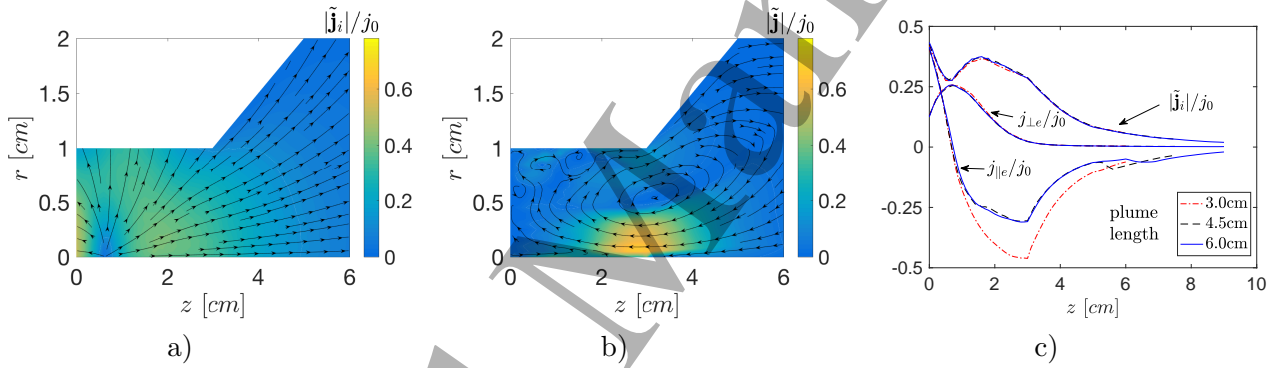


Figure 10: Panels (a) and (b) show ion and electric current densities for a case identical to C1A except that the plume axial length is 4.5cm instead of 3cm. For easier comparison with same currents in Fig. 4, plots have been restricted to $z \leq 6$ cm. Panel (c) compares ion and electron currents for plume axial lengths of 3cm, 4.5cm and 6cm, at the mean r of each $z = \text{constant}$ section.

4.5 Effects of mesh refinement

Simulations so far have been run on a MFAM (for the electrons) and a structured mesh (for the I-Module) of about 1200 cells each. To assess the solution sensitivity to mesh spacing, the case C1A with $T_{e0} = 16\text{eV}$ has been calculated with about 1200, 2400, and 4800 cells in each mesh. Increasing the number of cells is a costly process, since the time step has to be reduced as well to fulfill numerical stability; this makes the simulation time to increase nearly quadratically. To have an idea of the computational cost here, the base simulation of Fig. 4 with 1200 cells takes already about 12 hours in a machine with 12 cores (i.e. 6 days-core) to simulate 2.5ms.

Results of the mesh size sensitivity analysis are shown in Fig. 11. Figures 11(a) and 11(b) plot the electric current density in the case of 4800 cells for the two numerical choices on computing ϕ and must be compared with those of Fig. 9. As expected, smoother 2D maps are obtained as the mesh is refined. When algorithms work directly with Φ [subplot 11(a)], the differences on the current lines are small but the spatial irregularities on $|\tilde{\mathbf{j}}|$ of Fig. 9(a) have nearly disappeared. On the other hand, when working directly with ϕ [subplot 11(b)], irregularities decrease but still persist and there are still differences with subplot 11(a).

Figure 11(c) provides a more detailed evaluation of these results. It plots $|\tilde{\mathbf{j}}|$ at the exit section of the thruster ($z=3\text{cm}$) for the three mesh sizes and the two numerical strategies on computing ϕ . The convergence with the mesh size is observable and also the larger noise found when working directly with ϕ . A quantitative assessment of the differences among the curves is obtained taking first the case with 4800 cells and Φ as unknown as our ‘best (numerical) solution’. Then, calling $|\tilde{\mathbf{j}}|^{ref}(r)$ the curve for that case, the mean deviation of the rest of curves is defined as $\delta = 1/R \int_0^R ||\tilde{\mathbf{j}}|/|\tilde{\mathbf{j}}|^{ref} - 1| dr$ with $R=1\text{ cm}$. Values of this deviation (or apparent error) are given in the inserts of the two panels of Fig. 11(c). It is worth to notice that there is still a deviation of 9.3% with 4800 cells when working with ϕ , larger than in the case of 2400 cells and working with Φ .

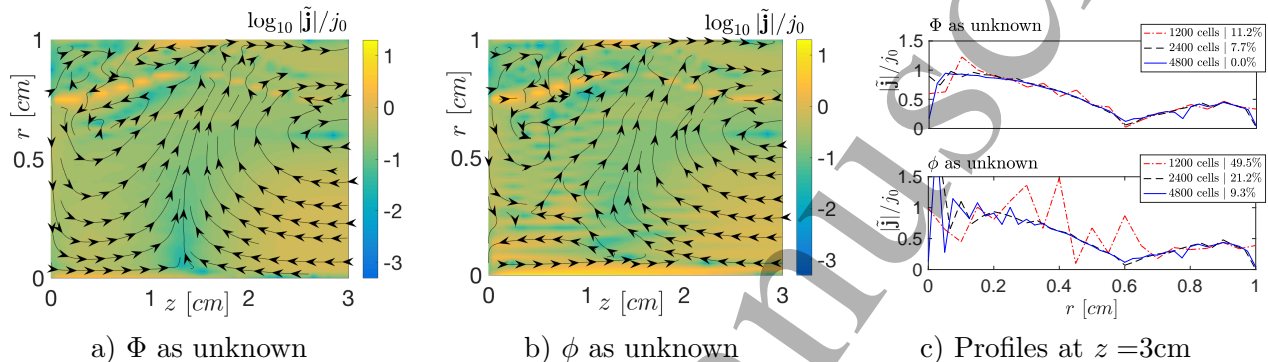


Figure 11: Panels (a) and (b) correspond to the same cases than Fig. 9 but using 4800 cells/mesh instead of 1200 in the simulations. Panel (c) plots the cuts of the electric current density at the chamber exit section, $z=3\text{cm}$, for the 1200, 2400 and 4800 cells/mesh cases and the two numerical strategies followed to compute ϕ . The percentages shown in the inserts of panel (c) correspond to the mean deviation δ (defined in the main text) with respect to $|\tilde{\mathbf{j}}|$ for 4800 cells and Φ as unknown.

5 Conclusions

The solution of a weakly-collisional, magnetized electron fluid model in a 2D axisymmetric geometry presents important challenges on magnitudes such as the electron current density, the ambipolar electric field, and the resulting electric potential map. These are caused by the large anisotropy between the directions parallel and perpendicular to the magnetic field, which can cause strong numerical diffusion ruining the accuracy of the results.

The first action for designing a reliable numerical treatment of that model is to operate on a magnetically aligned mesh, although this yields a large cell inhomogeneity in terms of size and aspect ratio. The second main action is to use a finite difference method for gradient reconstruction, whenever possible, which here means in all inner faces (i.e. those unrelated to boundary cells). It has been proven that weighted least squares methods, beyond presenting some arbitrariness on stencil and weight selection, can lead to numerical diffusion. Therefore, their use must be limited to the faces of the irregular boundary cells. Still, the computation of magnitudes in the boundary faces have required special modalities of the WLSM and there is still room for further improvements. Additionally, the use of a finite volume method for the electric current conservation equation has allowed to deal easily with the cells around singular null-points of the magnetic field.

The numerical methods on the electron model have been tested successfully by implementing them into the E-module of the HYPHEN code and simulating the plasma discharge in a HPT. The numerical benefits of using the thermalized potential instead of the natural electric potential, when solving the parallel Ohm’s law under large magnetization and low collisionality, have been assessed too. Variations of the thermalized potential are much lower than those of the electric potential, which allows to conclude (when a barotropy function exists) that the electric potential follows approximately a Boltzmann-type

relation with the plasma density. However, those variations are crucial in determining the parallel electron current density. Indeed, this current component has a central role in the formation of longitudinal electric current loops but these are shown to have a marginal effect on the rest of the plasma response. Related to this, it is also shown that the response is rather insensitive to the plume axial extension included in the simulation. Finally, the reliability of the solution against the number of cells used in the simulation, specially important in the case of an irregular magnetic mesh, has been checked positively.

The finite volume and gradient reconstruction methods on a MFAM have been analyzed here on a simplified polytropic electron model. The first next step is to add the electron energy and heat flux equations and to apply the algorithms developed here to them. The second next step is to match this electron transport model to the wave-plasma model and thus have a physically complete discharge in a HPT. Performances and optimization studies of HPTs will then be meaningful. In a parallel research line the application of this electron model and the HYPHEN code to Hall Effect Thruster discharges is also in progress [31].

Acknowledgements

The work of J. Zhou has been supported mainly by Airbus DS (CW240050) at Toulouse, France. The contributions of D. Pérez-Grande and P. Fajardo were supported mainly by the National Research and Development Program of Spain (partially with FEDER funds) under grant number ESP2016-75887-P. The work of E. Ahedo was supported mainly by the PROMETEO-CM project, funded by the Comunidad de Madrid, under Grant Y2018/NMT-4750 (including FEDER and FSE funds).

Appendix A Testing gradient reconstruction methods

The accuracy of the FDM and the WLSM for gradient reconstruction of Φ is tested here using the simple trial function

$$\psi(x_{\parallel}, x_{\perp}) = \exp(-x_{\parallel}/\bar{\chi}^2) \exp(-x_{\perp}), \quad (34)$$

where x_{\parallel} and x_{\perp} replicate the coordinates parallel and perpendicular to the magnetic field, the constant $\bar{\chi}$ replicates the Hall parameter and therefore controls the anisotropy level. The tests are performed at $x_{\parallel} = x_{\perp} = 0$ on the vertical face shown in Fig. 12 and compare the numerical and analytical values of $\partial\psi/\partial x_{\parallel}$ there. Left and right sketches in Fig. 12 show the stencils used for the FDM and the WLSM, respectively. The error on the numerical derivative (with subscript *num*) is

$$\varepsilon_{\parallel} = |\bar{\chi}^2(\partial\psi/\partial x_{\parallel})_{num} + 1|. \quad (35)$$

For the FDM two configurations of a 2-point stencil are used. In scheme FA, the cells are squares and identical with length $\Delta x_{\parallel} = \Delta x_{\perp} = 0.5$. In scheme FB, the left cell increases Δx_{\parallel} by a 10% compared to FA. The relative error ε_{\parallel} is shown in Fig. 12(left). Both in schemes FA and FB, the error decreases as $\sim \bar{\chi}^{-2}$ with $\bar{\chi}$ increasing. This means an excellent performance of the FDM, with the error being proportional to the second derivative of ψ . The higher error with the nonuniform FB is natural too. At very large $\bar{\chi}$ the error on FA reaches the machine precision.

Four schemes are used for assessing the relative error when using the WLSM. In scheme WA, an 8-point stencil with identical cells is used. In schemes WB and WC, the left cell changes Δx_{\parallel} by a 10% and a 1%, respectively. In scheme WD, the two upper cells change Δx_{\perp} by a 10%. The relative error ε_{\parallel} is shown in Fig. 12(right). Scheme WA behaves very well for any $\bar{\chi}$, but not as well as scheme FA. Scheme WD behaves exactly as WA, meaning that nonuniformities in the perpendicular direction do not matter. However, schemes WB and WC warn that nonuniformities in the parallel direction can lead to large errors at large $\bar{\chi}$. This is the numerical diffusion effect. Since the MFAM of our problem is highly nonuniform, it is concluded that the FDM must be used whenever it is possible.

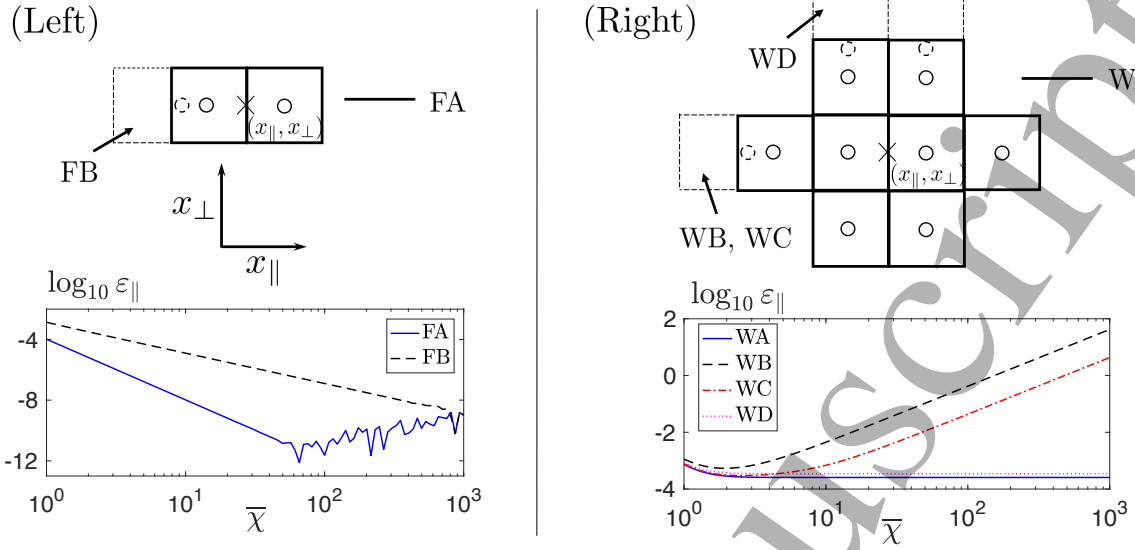


Figure 12: Scheme of the stencils used by each GRM when testing with the analytical function. Panel (left) corresponds to FDM and (right) to WLSM. GRM is done for a particular face of a hypothetical MFAM, which is represented by a cross and located at $(x_{\parallel}, x_{\perp})$. The surrounding cells, whose centers are marked by a circle, constitute the stencils. The main text explains the different configurations of the stencils.

Appendix B Performance indicators

The thrust produced by the plasma beam satisfies

$$F = \int_{W3} \sum_s (n_s m_s u_{zs} \mathbf{u}_s \cdot \mathbf{n} + n_s T_s \mathbf{1}_z \cdot \mathbf{n}) dS \quad (36)$$

with \mathbf{n} the external normal to surface W3. This thrust, with dynamic and static components, includes the contribution of both the heavy species (obtained through the I-module) and the electrons. The heavy species contribution to thrust is obtained from the I-module and is computed directly with the particle formulation and not with the above fluid one. Notice that if the simulated plume length is too short, the plasma beam acceleration would be incomplete and the thrust would be slightly underestimated.

The overall thrust efficiency is defined as

$$\eta_F = \frac{F^2}{2\dot{m}P_{abs}}, \quad (37)$$

where P_{abs} is the power absorbed by the plasma. There are several partial contributions to η_F , that are defined next. A steady-state discharge is assumed implicitly.

Let $\dot{m}_{i,W1}$, $\dot{m}_{i,W2}$, and $\dot{m}_{i,W3}$ be the mass flows of ions (of different electric charges) toward the surfaces W1, W2 and W3 of Fig. 1, and $\dot{m}_{i,total} = \dot{m}_{i,W1} + \dot{m}_{i,W2} + \dot{m}_{i,W3}$ the total ion flow produced by the thruster. The downstream ion flow $\dot{m}_{i,W3}$ is considered the useful one for thrust (except for fast neutrals). The quality of the plasma production in the chamber is characterized by the propellant utilization and the production efficiency, defined respectively as, [36]

$$\eta_u = \frac{\dot{m}_{i,W3}}{\dot{m}}, \quad \eta_{prod} = \frac{\dot{m}_{i,W3}}{\dot{m}_{i,total}}. \quad (38)$$

The production efficiency measures the percentage of the total plasma production useful for thrust; the rest of plasma production is just recombined at the walls.

In order to estimate a power budget and the power efficiency for this discharge, the energy balance of the whole plasma must be considered. Adding for all plasma species, the total energy equation can be expressed as

$$\nabla \cdot \sum_s \left[\left(\frac{5}{2} n_s T_s + \frac{1}{2} n_s m_s u_s^2 \right) \mathbf{u}_s + \mathbf{q}_s \right] = -\nabla \phi \cdot \mathbf{j} + Q_{abs} - Q_{ion} - Q_{exc}, \quad (39)$$

where: Q_{abs} is the density of power deposited; and Q_{ion} and Q_{exc} the power spent in ionization and excitation (inelastic collisions) per unit volume. Integrating the equation over the whole domain, the power balance is

$$P_{abs} = P_{ion} + P_{exc} + P_{W1} + P_{W2} + P_{W3}, \quad (40)$$

where P_{abs} , P_{ion} and P_{exc} are the volumetric integrals of Q_{abs} , Q_{ion} and Q_{exc} , respectively, and the three other integrals are energy flows through the different domain boundaries,

$$P_{W1} = \int_{W1} \sum_s \left[\left(\frac{5}{2} T_s + \frac{1}{2} m_s u_s^2 \right) n_s \mathbf{u}_s + \mathbf{q}_s \right] \cdot \mathbf{n} dS, \quad (41)$$

and identical expressions for walls W2 and W3. Equation (40) does not include the total work of the electric field on the domain since it is zero. This comes out from

$$\int_V \nabla \phi \cdot \mathbf{j} dV \equiv \int_{W1+W2+W3} \phi \mathbf{j} \cdot \mathbf{n} dS - \int_V \phi \nabla \cdot \mathbf{j} dV, \quad (42)$$

where: the first term at the right-hand side is zero if $j_n = 0$ at all surfaces, and the second term is zero since there are no sources of current inside the domain [Eq. (5)].

In the complete model of a HPT discharge, $Q_{abs}(z, r)$ will be determined from a wave-plasma sub-model, such as the one developed in [34]. Then, Eq. (39) would determine the 2D map of electron temperature. Here, since $T_e(z, r)$ has been prescribed through a polytropic relation with n_e , Eq. (39) is not used and, indeed, the power P_{abs} required to sustain that $T_e(z, r)$ is derived from Eq. (40).

Based on the useful power P_{W3} , the energy (or power) efficiency is defined as

$$\eta_{ene} = P_{W3}/P_{abs}. \quad (43)$$

The energy 'inefficiency' is evaluated through

$$\epsilon_{inel} = \frac{P_{ion} + P_{exc}}{P_{abs}}, \quad \epsilon_{wall} = \frac{P_{W1} + P_{W2}}{P_{abs}}, \quad (44)$$

which measure inelastic and wall losses, respectively.

Finally, there is the plume efficiency, measuring the effect of plume divergence. Here, this is defined as

$$\eta_{plu} = \frac{P_{zi,W3}}{P_{i,W3}}, \quad (45)$$

where $P_{zi,W3}$ and $P_{i,W3}$ are the flows of, respectively, axial and total energy of ions. Combining partial efficiencies, one has $\eta_F \approx \eta_u \eta_{ene} \eta_{plu}$.

References

- [1] R.W. Hockney and J.W. Eastwood. *Computer simulation using particles*. CRC Press, Boca Ratón, FL, 1988.
- [2] D. Tskhakaya, K. Matyash, R. Schneider, and F. Taccogna. The particle-in-cell method. *Contributions to Plasma Physics*, 47(8-9):563–594, 2007.
- [3] V. Vahedi and M. Surendra. A Monte Carlo collision model for the particle-in-cell method: applications to argon and oxygen discharges. *Computer Physics Communications*, 87(1-2):179–198, 1995.
- [4] C.P. Robert. *Monte Carlo methods*. John Wiley and Sons, Hoboken, NJ, 2004.
- [5] J.M. Fife. *Hybrid-PIC Modeling and Electrostatic Probe Survey of Hall Thrusters*. PhD thesis, 1998.
- [6] J.C. Adam, A. Herón, and G. Laval. Study of stationary plasma thrusters using two-dimensional fully kinetic simulations. *Physics of Plasmas*, 11:295–305, 2004.
- [7] F. Taccogna, R. Schneider, S. Longo, and M. Capitelli. Kinetic simulations of a plasma thruster. *Plasma Sources Science and Technology*, 17(2):024003, 2008.
- [8] I.D. Kaganovich, Y. Raitses, D. Sydorenko, and A. Smolyakov. Kinetic effects in a Hall thruster discharge. *Physics of Plasmas*, 14:057104, 2007.
- [9] K. Komurasaki, K. Mikami, and Y. Arakawa. Two-dimensional numerical model of plasma flow in a Hall thruster. *J. Propulsion Power*, 11(6):1317–1323, 1995.
- [10] J.M. Fife and M. Martinez-Sanchez. Comparison of results from a two-dimensional numerical spt model with experiment. In *32nd Joint Propulsion Conference, Lake Buena Vista, FL, AIAA-1996-3197*, 1996.
- [11] J.P. Boeuf and L. Garrigues. Low frequency oscillations in a stationary plasma thruster. *J. Applied Physics*, 84(7):3541–3554, 1998.
- [12] J Bareilles, GJM Hagelaar, L Garrigues, C Boniface, JP Boeuf, and N Gascon. Critical assessment of a two-dimensional hybrid hall thruster model: Comparisons with experiments. *Physics of Plasmas*, 11(6):3035–3046, 2004.
- [13] J.W. Koo and I.D. Boyd. Computational model of a Hall thruster. *Computer physics communications*, 164:442–447, 2004.
- [14] F.I. Parra, E. Ahedo, M. Fife, and M. Martínez-Sánchez. A two-dimensional hybrid model of the Hall thruster discharge. *Journal of Applied Physics*, 100:023304, 2006.
- [15] D. Escobar and E. Ahedo. Two-dimensional electron model for a hybrid code of a two-stage Hall thruster. *IEEE Transactions on Plasma Science*, 36:2043–2057, 2008.
- [16] E. Ahedo, R. Santos, and F. Parra. Fulfillment of the kinetic Bohm criterion in a quasineutral particle-in-cell model. *Physics of Plasmas*, 17(7):073507, 2010.
- [17] R.R. Hofer, P.Y. Peterson, A.D. Gallimore, and R.S. Jankovsky. A high specific impulse two-stage Hall thruster with plasma lens focusing. In *7th International Electric Propulsion Conference, Pasadena, CA, USA, IEPC-01-036*, 2001.

- [18] Michael Keidar and Isak I Beilis. Sheath and boundary conditions for plasma simulations of a hall thruster discharge with magnetic lenses. *Applied Physics Letters*, 94(19):191501, 2009.
- [19] N. Koch and M. Schirra. The HEMPT concept - a survey on theoretical considerations and experimental evidences. In *32nd International Electric Propulsion Conference*, paper 2011-236, Wiesbaden, Germany, September 11-15, 2011. Electric Rocket Propulsion Society, Fairview Park, OH.
- [20] I.G. Mikellides, I. Katz, R.R. Hofer, D.M. Goebel, K. de Grys, and A. Mathers. Magnetic shielding of the channel walls in a Hall plasma accelerator. *Physics of Plasmas*, 18:033501, 2011.
- [21] Ioannis G Mikellides, Ira Katz, Richard R Hofer, and Dan M Goebel. Magnetic shielding of a laboratory hall thruster. i. theory and validation. *Journal of Applied Physics*, 115(4):043303, 2014.
- [22] E. Ahedo and Mario Merino. Two-dimensional supersonic plasma acceleration in a magnetic nozzle. *Physics of Plasmas*, 17(7):073501, 2010.
- [23] I.G. Mikellides and I. Katz. Numerical simulations of hall-effect plasma accelerators on a magnetic-field-aligned mesh. *Physical Review E*, 86(4):046703, 2012.
- [24] Ioannis G Mikellides and Alejandro Lopez Ortega. 2d (r-z) numerical simulations of the plasma and channel erosion in a 100kw class nested hall thruster. *Plasma Sources Science and Technology*, 27:075001, 2018.
- [25] Ioannis G Mikellides and Alejandro Lopez Ortega. Challenges in the development and verification of first-principles models in hall-effect thruster simulations that are based on anomalous resistivity and generalized ohm's law. *Plasma Sources Science and Technology*, 28:014003, 2019.
- [26] A Lopez Ortega, Ioannis G Mikellides, and Vernon H Chaplin. Numerical simulations for the assessment of erosion in the 12.5-kw hall effect rocket with magnetic shielding (hermes). In *35th International Electric Propulsion Conference, Atlanta, GA, IEPC-2017-154*, 2017.
- [27] S.J. Araki and R.E. Wirz. Cell-centered particle weighting algorithm for pic simulations in a non-uniform 2d axisymmetric mesh. *Journal of Computational Physics*, 272:218–226, 2014.
- [28] D. Pérez-Grande, O. González-Martínez, P. Fajardo, and E. Ahedo. Analysis of the numerical diffusion in anisotropic mediums: benchmarks for magnetic field aligned meshes in space propulsion simulations. *Applied Sciences*, 6(11):354, 2016.
- [29] F. Cichocki. *Analysis of the expansion of a plasma thruster plume into vacuum*. PhD thesis, Universidad Carlos III de Madrid, Leganés, Spain, 2017.
- [30] Adrián Domínguez-Vázquez, Francesco Taccogna, P. Fajardo, and E. Ahedo. Influence of relevant parameters on the radial PIC simulation of a Hall effect thruster discharge. In *Space Propulsion Conference 2018*, number 00288, Seville, Spain, May 14-18, 2018. Association Aéronautique et Astronautique de France.
- [31] Adrián Domínguez-Vázquez. *Axisymmetric simulation codes for Hall effect thrusters and plasma plumes*. PhD thesis, Universidad Carlos III de Madrid, Leganés, Spain, To be defended, 2019.
- [32] E. Ahedo and V. de Pablo. Combined effects of electron partial thermalization and secondary emission in Hall thruster discharges. *Physics of Plasmas*, 14:083501, 2007.
- [33] D. Pérez-Grande. *Fluid modeling and simulation of the electron population in Hall effect thrusters with complex magnetic topologies*. PhD thesis, Universidad Carlos III de Madrid, Leganés, Spain, 2018.

- [34] Bin Tian, Mario Merino, and E. Ahedo. Two-dimensional plasma-wave interaction in an helicon plasma thruster with magnetic nozzle. *Plasma Sources Science and Technology*, 27(11):114003, 2018.
- [35] Á. Sánchez-Villar and Mario Merino. Advances in wave-plasma modelling in ECR thrusters. In *Space Propulsion Conference 2018*, number 00346, Seville, Spain, 2018. Association Aéronautique et Astronautique de France.
- [36] E. Ahedo and J. Navarro-Cavallé. Helicon thruster plasma modeling: Two-dimensional fluid-dynamics and propulsive performances. *Physics of Plasmas*, 20(4):043512, 2013.
- [37] Kazunori Takahashi, Trevor Lafleur, Christine Charles, Peter Alexander, and Rod W Boswell. Axial force imparted by a current-free magnetically expanding plasma. *Physics of Plasmas*, 19(8):083509, 2012.
- [38] J Navarro-Cavallé, M Wijnen, P Fajardo, and E Ahedo. Experimental characterization of a 1 kw helicon plasma thruster. *Vacuum*, 149:69–73, 2018.
- [39] F. Trezzolani, A. Lucca Fabris, D. Pavarin, et al. Low power radio-frequency plasma thruster development and testing. In *33th International Electric Propulsion Conference, IEPC 2013-153*, 2013.
- [40] F. Cichocki, Mario Merino, and E. Ahedo. A 3d electron fluid model to study magnetic field effects on an expanding plasma thruster plume. In *Space Propulsion Conference 2018*, number 00295, Seville, Spain, May 14-18, 2018. Association Aéronautique et Astronautique de France.
- [41] Schenk O. Lubin M. & Gärtner K. Petra, C. G. An augmented incomplete factorization approach for computing the schur complement in stochastic optimization. *SIAM Journal on Scientific Computing*, 36(2):C139–C162, 2014.
- [42] Schenk O. & Anitescu M. Petra, C. G. Real-time stochastic optimization of complex energy systems on high-performance computers. *Computing in Science & Engineering*, 16(5):32–34, 2014.
- [43] H. Kotakemori, H. Hasegawa, and A. Nishida. Performance evaluation of a parallel iterative method library using openmp. In *Eighth International Conference on High-Performance Computing in Asia-Pacific Region (HPCASIA'05)*, paper 5-pp. IEEE, 2005.
- [44] Boris Diskin and James L Thomas. Effects of mesh regularity on accuracy of finite-volume schemes. In *50th AIAA Aerospace Sciences Meeting*, pages 2012–0609, 2012.
- [45] E. Shima, K. Kitamura, and T. Haga. Green-gauss/weighted-least-squares hybrid gradient reconstruction for arbitrary polyhedra unstructured grids. *AIAA Journal*, 51(11):2740 – 2747, 2013.
- [46] E. Sozer, C. Brehm, and C.C. Kiris. Gradient calculation methods on arbitrary polyhedral unstructured meshes for cell-centered cfd solvers. In *52nd Aerospace Sciences Meeting*, National Harbor, Maryland, US, 2014.
- [47] T Lafleur, F Cannat, J Jarrige, PQ Elias, and D Packan. Electron dynamics and ion acceleration in expanding-plasma thrusters. *Plasma Sources Science and Technology*, 24(6):065013, 2015.
- [48] JM Little and EY Choueiri. Electron cooling in a magnetically expanding plasma. *Physical Review Letters*, 117(22):225003, 2016.
- [49] Min Li, Mario Merino, E. Ahedo, and Haibin Tang. On electron boundary conditions in PIC plasma thruster plume simulations. *Plasma Sources Science and Technology*, 28(03):034004, 2019. doi:10.1088/1361-6595/ab0949.

- 1
2 [50] E. Ahedo. Parametric analysis of a magnetized cylindrical plasma. *Physics of Plasmas*,
3 16(11):113503, 2009.
4
5 [51] T. Lafleur. Helicon plasma thruster discharge model. *Physics of Plasmas*, 21(4):043507, 2014.
6
7 [52] Kazunori Takahashi, Christine Charles, and Rod Boswell. Approaching the theoretical limit of
8 diamagnetic-induced momentum in a rapidly diverging magnetic nozzle. *Physical review letters*,
9 110(19):195003, 2013.
10
11 [53] JM Little and EY Choueiri. Critical condition for plasma confinement in the source of a magnetic
12 nozzle flow. *IEEE Transactions on Plasma Science*, 43(1):277–286, 2014.
13
14 [54] F. Cichocki, Adrián Domínguez-Vázquez, Mario Merino, and E. Ahedo. Hybrid 3D model for the
15 interaction of plasma thruster plumes with nearby objects. *Plasma Sources Science and Technology*,
16 26(12):125008, 2017.
17
18 [55] E. Ahedo and Mario Merino. Two-dimensional plasma expansion in a magnetic nozzle: separation
19 due to electron inertia. *Physics of Plasmas*, 19(8):083501, 2012.
20
21 [56] Mario Merino and E. Ahedo. Fully magnetized plasma flow in a magnetic nozzle. *Physics of Plasmas*,
22 23(2):023506, 2016. doi:10.1063/1.4941975.
23
24
25
26
27
28
29
30
31
32
33
34
35
36
37
38
39
40
41
42
43
44
45
46
47
48
49
50
51
52
53
54
55
56
57
58
59
60